

## Rayleigh-Taylor instability with magnetic fluids: Experiment and theory

G. Pacitto,<sup>1,2,\*</sup> C. Flament,<sup>1,2</sup> J.-C. Bacri,<sup>1,2</sup> and M. Widom<sup>3,1</sup>

<sup>1</sup>*Université Paris 7–Denis Diderot, UFR de Physique (Case 7008), 2 place Jussieu, 75251 Paris Cedex 05, France*

<sup>2</sup>*Laboratoire des Milieux Désordonnés et Hétérogènes (Case 78), Université Paris 6–UMR 7603 CNRS, 4 place Jussieu, 75252 Paris cedex 05, France*

<sup>3</sup>*Department of Physics, Carnegie Mellon University, Pittsburgh, Pennsylvania 15213*

(Received 12 July 2000)

We present experiments showing the Rayleigh-Taylor instability at the interface between a dense magnetic liquid and an immiscible less dense liquid. The liquids are confined in a Hele-Shaw cell and a magnetic field is applied perpendicular to the cell. We measure the wavelength and the growth rate at the onset of the instability as a function of the external magnetic field. The wavelength decreases as the field increases. The amplitude of the interface deformation grows exponentially with time in the early stage, and the growth rate is an increasing function of the field. These results are compared to theoretical predictions given in the framework of linear stability analysis.

PACS number(s): 47.20.Ma, 75.50.Mm

### I. INTRODUCTION

When a dense fluid lies above a less dense fluid, a gravitational instability, called the Rayleigh-Taylor instability (RTI) [1,2], causes fingering at the interface between the fluids. Rising fingers of the lighter fluid penetrate the heavier fluid and, conversely, fingers of the heavier fluid fall into the lighter one. In three dimensions, the fingers of each fluid take place at the vertices of a hexagonal lattice on the two-dimensional interface [3]. In a Hele-Shaw cell, modeling a quasi-two-dimensional system, the one-dimensional interface is destabilized by the growth of fingers regularly spaced on a line with a well-defined wavelength. This wavelength results from the competition between the stabilizing capillary force, and the destabilizing gravitational force. At the threshold of the instability, the wavelength,  $\lambda_0$  is proportional to the capillary length  $\lambda_0 = 2\sqrt{3}\pi l_c$ , with  $l_c = \sqrt{\gamma/\Delta\rho g}$  where  $\gamma$  is the surface tension,  $\Delta\rho > 0$  is the density difference between the two fluids, and  $g$  is the gravitational acceleration. This instability plays an important role in subjects such as astrophysics, fusion and turbulence [4–6]. Although the phenomenon has been studied for decades, much remains to be learned about it.

The development of patterns resulting from the RTI can be divided into three stages: the early linear stage, where the lengths of the rising and falling fingers are small compared to the wavelength, the middle, weakly nonlinear stage, and the strongly nonlinear late stage. The linear stage is well described but to our knowledge, no experiment has been achieved to verify this behavior. The nonlinear stages are not fully understood.

Several theoretical studies start from the Navier-Stokes equation and perform a linear analysis of the instability [7,8]. Particular issues studied address the compressibility of the fluids [9,10], density gradients [7,11], and viscosity effects [7,8,12–14]. In the nonlinear regime, Ott [15], Baker and Freeman [16], and Crowley [17] describe the motion of the

fingers. Studies using miscible fluids, performed by Petitjeans and Kurowski [18] observe similarities with immiscible fluids in the development of the instability, even though the wavelength and the growth rate differ greatly. They believe the similarity arises because the density gradient between the two fluids acts like an equivalent surface tension at the onset of the instability. Authelin, Brochard, and de Gennes [19] describe the interface melting of two miscible fluids by the RTI. This instability generates micron-sized drops that then dissipate by diffusion.

One of us [20], used a mode-coupling analysis of Darcy's law to describe the weakly nonlinear evolution of the viscous fingering patterns obtained in a Hele-Shaw cell. This study, describing the RTI is also applicable for the Saffman-Taylor instability (STI) [21], with a low viscosity fluid pushing a more viscous one in a Hele-Shaw cell.

Recent works [22] determine the length scale of the fingers, show a difference between the width of the rising fingers and the width of the falling fingers, and explain their amalgamation in terms of spatial modulations. For miscible fluids, the turbulent mixing zone is numerically studied by Youngs in 2D [23] and 3D [24], and experimentally by Read [25]. Ratafia [26] studied the nonlinear regime, and described the destabilization of fingers by the presence of Kelvin-Helmholtz instability (KHI) [27], resulting from the jump of the tangential velocity between the two fluids at the edges of the fingers. This interpretation can explain the fractal structure obtained after nonlinear evolution, which is the result of a KHI cascade.

Recent Rayleigh-Taylor experiments using a mixture of water and sand [28], modeled as a Newtonian fluid, determine the viscosity of the suspension, and find results in agreement with other experimental measurements. To our knowledge, this RTI experiment is the only experiment that uses complex media.

Magnetic fluids (MF, also called ferrofluids) are stable colloidal suspensions of magnetic nanoparticles. An applied magnetic field provides a new external parameter that can stabilize or destabilize the fluid interface, causing interesting hydrodynamic instabilities. One can distinguish two kinds of

\*Email address: pacitto@ccr.jussieu.fr

instabilities in ferrofluids: static instabilities caused by the magnetic field, which are not present in ordinary fluids; and dynamic instabilities that appear or are modified by applied fields.

The first static instability observed in MF is the peak instability [29]. A static magnetic external field  $H_{\text{ext}}$  applied tangent to a free surface generally stabilizes the surface. However,  $H_{\text{ext}}$  applied normal to a horizontal surface causes the peak instability to rise above a critical value of  $H_{\text{ext}}$ . A line (in 2D) or a lattice (in 3D) of spikes arises from the competition between the destabilizing magnetic forces and the stabilizing capillary and gravitational forces.

Now, let the MF be confined in a two-dimensional Hele-Shaw cell. Another instability can appear if the external field is applied in the direction perpendicular to the cell. This phenomenon, called the labyrinthine instability [30,31], occurs above a critical value of the applied field and with a critical wavelength. The threshold value of  $H_{\text{ext}}$  results from a balance between the destabilizing magnetic dipole-dipole repulsion and the stabilizing surface tension (and possibly gravity in a vertical cell).

MF can be used as a dynamic system if a time-dependent magnetic field is applied. Different surface phenomena are observed such as surface waves [32,33], the Faraday instability [34], or a period doubling in the case of the peak instability [35].

Hydrodynamic instabilities may occur when the MF flows. For example, Saffman-Taylor fingering has been studied, both experimentally and theoretically, with an MF. In this configuration, the external magnetic field can be applied normal to, or within the plane of the cell. The situation is stabilizing if  $H_{\text{ext}}$  is tangent to the interface within the plane of the cell [36]. Experiments performed with a field applied in a direction perpendicular to a circular Hele-Shaw cell show a destabilizing behavior [37].

The aim of this paper is to study the influence of a homogeneous magnetic field applied perpendicular to a vertical Hele-Shaw cell filled with a dense water-based ferrofluid above a lighter oil. In a recent paper [38], one of us describes theoretically the general viscous fingering pattern obtained in this configuration. In this dynamic situation, the magnetic force is added to the gravitational force to destabilize the interface, while the capillary effects stabilize it.

## II. LINEAR STABILITY ANALYSIS

Consider a vertical Hele-Shaw cell of gap  $h$  filled with oil of density  $\rho_-$  and viscosity  $\eta_-$  at the bottom and an immiscible MF of density  $\rho_+$  and viscosity  $\eta_+$  on top. We use a coordinate system in which the Hele-Shaw cell lies parallel to the  $xy$  plane, the  $y$  axis is vertically upward, and the  $z$  axis is perpendicular to the Hele-Shaw cell. Gravity acts downward parallel to the  $y$  axis and a uniform external magnetic field  $\vec{H}_{\text{ext}} = H_{\text{ext}}\hat{z}$ , is parallel to the  $z$  axis (see Fig. 1). We present equations of motion and boundary conditions and then we perform a linear stability analysis of these equations. We show that both gravitational (provided  $\rho_+ > \rho_-$ ) and magnetic instabilities deform an initially flat interface.

To begin, we derive Darcy's law for the flow of MF. The analysis begins with the basic equation governing the three-dimensional fluid flow  $\vec{v}(x,y,z)$ , the Navier-Stokes equation

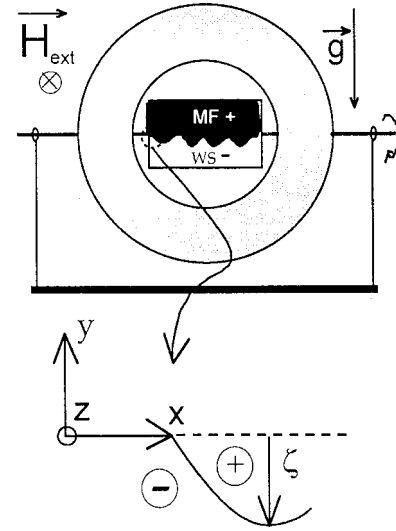


FIG. 1. The experimental setup consists in a cell located vertically between two coils. The external magnetic field obtained is horizontal and perpendicular to the cell. The cell that contains the both liquids can be rotated around a horizontal axis.

$$\rho \frac{D\vec{v}}{Dt} = -\vec{\nabla}p + \rho\vec{g} + \eta\vec{\Delta}\vec{v} + \vec{f}_m. \quad (1)$$

From this equation, we derive Darcy's law assuming sufficiently high viscosity so that the flow velocity is small, so the inertial term on the left-hand side may be neglected. The idea is to average Eq. (1) over the gap, resulting in a 2D flow equation for the gap-averaged velocity  $\vec{u}$ . The gap average of the three-dimensional pressure gradient yields a two-dimensional gradient of the gap-averaged pressure, which we continue to represent as  $\vec{\nabla}p$ . As is usual in derivations of Darcy's law, the gap average of the viscous drag force, subject to no-slip boundary conditions imposed at  $z = \pm h/2$ , is  $-(12\eta/h^2)\vec{u}$ .

The final term in Eq. (1),  $\vec{f}_m = \mu_0(\vec{M} \cdot \vec{\nabla})\vec{H}$ , represents the magnetic body force on a fluid element, neglecting compressibility and self-induction of the fluid [39]. In this approximation,  $\vec{M}$  is constant and parallel to  $z$ , and the gap average of  $f_m$  reduces to  $(\mu_0 M/h)[H(x,y,h/2) - H(x,y,-h/2)]$ . Because the applied field  $\vec{H}_{\text{ext}}$  is spatially uniform, it drops out of this difference and the magnetic force arises entirely from the demagnetizing field  $\vec{H}_d = \vec{H} - \vec{H}_{\text{ext}}$  caused by the surface magnetic poles. Express the demagnetizing field as the gradient of a magnetic scalar potential,  $\vec{H}_d = -\vec{\nabla}\psi(x,y,z)$ , and take  $\psi$  as an odd function of  $z$ . The gap average of the magnetic force is  $\vec{f}_m = -(2\mu_0 M/h)\vec{\nabla}\psi(x,y,h/2)$ , where now the gradient acts only on  $x$  and  $y$  coordinates [40].

Collect all averaged terms and isolate the velocity  $\vec{u}$  on the left-hand side,

$$\frac{12\eta}{h^2}\vec{u} = -\vec{\nabla}p - \rho g\hat{y} - \mu_0 \frac{2M}{h}\vec{\nabla}\psi(x,y). \quad (2)$$

Here all vectors lie in the  $xy$  plane, and the scalar potential  $\psi(x,y) \equiv \psi(x,y,h/2)$  is evaluated at the top plate. Further

simplification of Darcy's law (2) occurs if we exploit the irrotational flow to introduce the velocity potential  $\vec{u} = -\vec{\nabla}\phi$  so that

$$\frac{12\eta}{h^2}\phi = p + \rho gy + \mu_0 \frac{2M}{h}\psi(x, y). \quad (3)$$

Now we apply Darcy's law (3) within each fluid evaluated at the interface between the two fluids,  $y = \zeta(x)$ . Subtract Eq. (3) for the oil (fluid  $-$ ) from the same equation for MF (fluid  $+$ ) and find

$$\begin{aligned} & A \left( \frac{\phi_+ + \phi_-}{2} \right) + \left( \frac{\phi_+ - \phi_-}{2} \right) \\ &= \frac{h^2}{12(\eta_- + \eta_+)} \left( (p_+ - p_-) + \mu_0 \frac{2M}{h}\psi \right) \\ & \quad + \frac{h^2(\rho_+ - \rho_-)g}{12(\eta_+ + \eta_-)}\zeta \end{aligned} \quad (4)$$

for the viscosity contrast  $A = (\eta_+ - \eta_-)/(\eta_+ + \eta_-)$ . The pressure jump across the interface,  $p_+ - p_-$ , is the surface tension  $\gamma$  times the mean interface curvature  $\kappa$ . For a thin gap  $h$ , we need only consider the curvature of  $\zeta(x)$ , which we may approximate  $\kappa \approx \partial^2\zeta/\partial x^2$  for the purpose of linear stability analysis [38].

Represent the net perturbation  $\zeta(x, t)$  in the form of a Fourier mode

$$\zeta(x, t) = \zeta'_k(t) \cos(kx). \quad (5)$$

The velocity potentials  $\phi_{\pm}$  must obey Laplace's equation  $\nabla^2\phi_{\pm} = 0$ , because the fluids are incompressible. The boundary conditions at  $y \rightarrow \pm\infty$ , so that  $\nabla\phi_{\pm} = 0$ . We give  $\phi_{\pm}$  the appropriate wavevector and phase to be consistent with the perturbation  $\zeta$ . The general velocity potentials obeying these requirements are

$$\phi_{\pm}(x, y, t) = \phi_{\pm k} \exp(\mp ky) \cos(kx). \quad (6)$$

In order to substitute expansions (6) into the equation of motion (4), we need to evaluate them at the perturbed interface. To first order in the perturbation, it suffices to simply set  $y = 0$  in Eq. (6).

To close Eq. (4) we need additional relations expressing the velocity potentials in terms of the perturbation amplitudes. To find these, consider the kinematic boundary condition that the interface moves according to the local fluid velocities. To first order in  $\zeta$ , we simply note  $\partial\zeta/\partial t = -\partial\phi_i/\partial y$  [38]. Substituting Eq. (6) for  $\phi_{\pm}$  and Fourier transforming yields  $\zeta_k = -k\phi_{k-} = k\phi_{k+}$ . Then Eq. (4) reads

$$\begin{aligned} \frac{1}{k} \frac{\partial\zeta_k}{\partial t} &= \frac{h^2}{12(\eta_- + \eta_+)} \left( -\gamma k^2 \zeta_k + \mu_0 \frac{2M}{h} \psi_k \right) \\ & \quad + \frac{h^2(\rho_+ - \rho_-)g}{12(\eta_- + \eta_+)} \zeta_k \end{aligned} \quad (7)$$

To obtain the Fourier transform of the magnetic scalar potential,  $\psi_k$ , we write the magnetic scalar potential

$$\begin{aligned} \psi(x, y) &= \frac{M}{4\pi} \int_{-\infty}^{\infty} dx' \int_{\zeta(x')}^{\infty} dy' \left[ \frac{1}{\sqrt{(x-x')^2 + (y-y')^2}} \right. \\ & \quad \left. - \frac{1}{\sqrt{(x-x')^2 + (y-y')^2 + h^2}} \right]. \end{aligned} \quad (8)$$

The expansion of  $\psi(x, \zeta(x))$  to first order in  $\zeta$  is

$$\begin{aligned} \psi(x) &= \psi_0 + \frac{M}{4\pi} \int_{-\infty}^{\infty} dx' \left( \frac{1}{\sqrt{(x-x')^2}} - \frac{1}{\sqrt{(x-x')^2 + h^2}} \right) \\ & \quad \times [s(x') - s(x)] \end{aligned} \quad (9)$$

and its Fourier transform  $\psi_k = 2MJ(kh)\zeta_k$ , where

$$J(x) \equiv \ln(x/2) + K_0(x) + C_{\text{Euler}} \quad (10)$$

with where  $K_0$  a Bessel function and  $C_{\text{Euler}} = 0.5772\dots$  is the Euler constant [41].

Inserting  $\psi_k$  into Eq. (7) for the growth of the cosine mode, the differential equation of the interface is

$$\dot{\zeta}_k = \sigma(k)\zeta_k, \quad (11)$$

where

$$\sigma(k) = kV_c [B_G + 2B_M J(kh) - (kh)^2] \quad (12)$$

is the linear growth rate multiplying the first-order term in  $\zeta$  with  $V_c = \gamma/12(\eta_+ + \eta_-)$  as the capillary velocity,  $B_G = (\rho_+ - \rho_-)gh^2/\gamma$  the gravitational Bond number, and

$$B_M = \left( \frac{\mu_0}{4\pi} \right) \frac{2M^2 h}{\gamma}$$

is the magnetic Bond number. An asymptotic expression for  $kh \ll 1$  that is more convenient for the data analysis can be obtained by expanding  $J(kh)$  for small  $kh$  [42]:

$$J(kh) \approx \frac{(kh)^2}{4} [1 - C_{\text{Euler}} - \ln(kh/2)]. \quad (13)$$

### III. EXPERIMENTAL SETUP

The experimental geometry is sketched in Fig. 1. The cell is located in a gap between two coils in the Helmholtz configuration to achieve good axial homogeneity for the magnetic field  $\vec{H}_{\text{ext}}$ . The radial homogeneity of the field is better than 3%. The amplitude of the external field is nearly constant. The cell is mounted so it can be rotated around the  $x$  axis, which passes through the middle of the gap.

We use an ionic magnetic fluid made of cobalt ferrite particles ( $\text{CoFe}_2\text{O}_4$ ) dispersed in a mixture of water and glycerol. This MF is synthesized by Neveu [43] following the Massart's method [44]. The magnetization of the MF as a function of  $H_{\text{ext}}$  is obtained by the use of a calibrated fluxmeter.

The rectangular cell consists of two parallel plates made of altuglass (Plexiglas) with a spacing between the two plates of  $h = 500 \mu\text{m}$ . The cell is initially filled with an oil (White Spirit or WS) of low density (compared to the MF) that wets

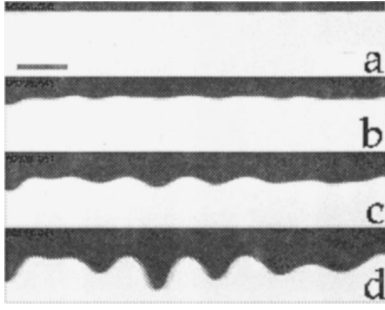


FIG. 2. Several pictures of the destabilizing MF-WS interface for different times (a)  $t=0$ ; (b)  $t=5$  s; (c)  $t=8$  s; (d)  $t=11$  s for  $H_{\text{ext}}=7.9$  kA/m. The gray bar equals 1 cm.

the altuglass walls. A thin film (of micron width) of WS separates the MF from the walls, avoiding pinning of the MF-WS contact line on the walls.

The mass density of MF is  $\rho_+ = 1686 \pm 85$  kg m $^{-3}$ , compared to  $\rho_- = 800$  kg m $^{-3}$  for WS. The dynamic viscosity of the MF is  $\eta_+ = 0.14$  kg m $^{-1}$  s $^{-1}$  at room temperature. The viscosity of the WS is two orders of magnitude lower, so we may take  $\eta_- \approx 0$ .

Image processing is used to measure the wavelength and the growth increment. The images are recorded by a CCD camera (charge-coupled device) and digitized by an acquisition card in a computer. We use the public domain software NIH Image [45] to analyze the images.

## IV. RESULTS

### A. Wavelength measurements

The experiments are conceptually simple: the cell is placed vertically with the heavier liquid (MF) below. We rotate the cell by 180° around the  $x$  axis and apply the magnetic field. The selected wavelength depends on how and when the magnetic field is applied. If  $H_{\text{ext}}$  is applied during the rotation, we get a different measurement than if  $H_{\text{ext}}$  is switched on at the end of the rotation. The response of the MF-WS interface to the magnetic field is usually much faster than its response to a gravitational field. That is, a longer time is needed to observe the classical RTI without an external magnetic field than to observe the labyrinthine instability [30,31]. If  $H_{\text{ext}}$  is applied during rotation when the cell is momentarily horizontal, the normal field instability [29] appears before the RTI. To avoid these difficulties, we apply the field only after the rotation is complete, but before the RTI appears. The duration of rotation is about 1 s, and the time constant for ramping up the magnetic field is less than 1 s.

We collected data for 13 different values of  $H_{\text{ext}}$ , with two independent runs for each value of  $H_{\text{ext}}$ . The wavelength  $\lambda_0 = 2\pi/k_0$ , is measured at the onset of the instability until the amplitude  $\zeta$  of the interface deformation remains small:  $k_0\zeta < 0.1$ . We compared two different methods: a FFT of the interface gives the fundamental mode  $k_0$ , a direct measurement of the average peak to peak distance gives  $\lambda_0$ . In the second approach, we reject the peaks located close to the edges of the cell, and we omit certain peaks that are dominated by others (“finger competition”). Both methods give similar results within the errors bars.

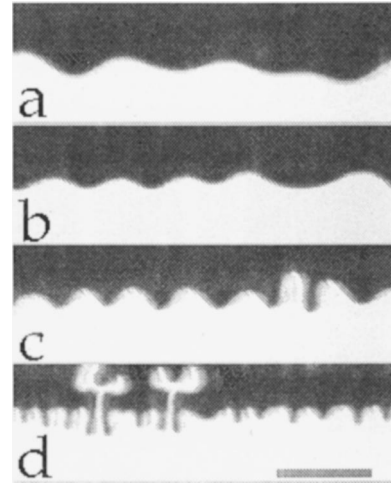


FIG. 3. Several destabilizing interfaces for different values of the applied field (a)  $H_{\text{ext}}=4.1$  kA/m and  $t=8$  s; (b)  $H_{\text{ext}}=11.9$  kA/m and  $t=9$  s; (c)  $H_{\text{ext}}=17.8$  kA/m and  $t=6$  s;  $H_{\text{ext}}=31.6$  kA/m and  $t=1$  s. The gray bar equals 1 cm.

Figure 2 displays a sequence of pictures of the destabilizing MF-WS interface for  $H_{\text{ext}}=7.9$  kA/m. A comparison of interfaces for different values of the external field is shown in Fig. 3. Both the wavelength and the width of the MF fingers decrease as  $H_{\text{ext}}$  increases. The experimental values of  $\lambda_0$  as a function of the external field  $H_{\text{ext}}$  are reported in Fig. 4.

To compare experimentally observed wavelengths with the linear stability analysis, consider the growth rate,  $\sigma(k)$ . Maximizing expression (12) for  $\sigma(k)$  versus the wavevector, gives the fastest growing mode  $k_0$ :

$$\left( \frac{\partial \sigma}{\partial k} \right)_{k=k_0} = 0 \Leftrightarrow \lambda_0 = \frac{2\pi}{k_0}.$$

We get the following nonalgebraic equation:

$$\frac{B_G}{4\pi^2} x_0^2 + B_M \left[ a + \frac{3}{2} \ln(x_0) \right] - 3 = 0, \quad (14)$$

with,  $a = 1 - \frac{3}{2} C_{\text{Euler}} - \frac{3}{2} \ln(\pi) \approx -0.79$ , and  $x_0 = \lambda_0/h$ . To determine the value of

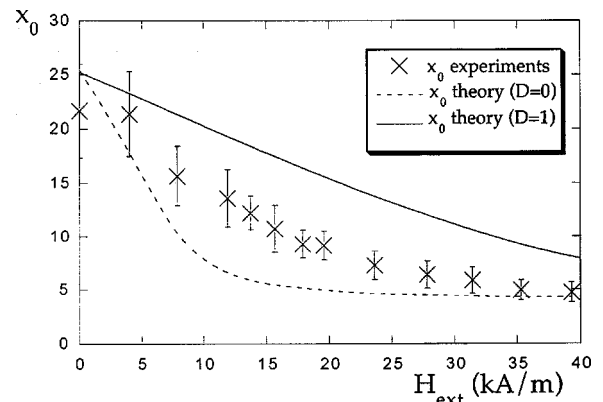


FIG. 4. Wavelength as a function of the external applied field  $H_{\text{ext}}$ . Experimental data are measured by the direct peak-to-peak method, at the onset of the instability.

$$B_M = \frac{\mu_0}{4\pi} \frac{2M^2 h}{\gamma}$$

for a given value of  $H_{\text{ext}'}$ , we need to know the MF-WS surface tension  $\gamma$ . The value of  $\gamma$  can be deduced from the wavelength at the onset of the RTI with  $H_{\text{ext}}=0$  using formula (12). We find  $\gamma=8.6\pm 3.8\text{ mN m}^{-1}$  by this method. We can also determine the value of  $\gamma$  from the wavelength at the threshold of the normal field instability, which is linked with the capillary length [46]. This method yields  $\gamma=12.0\pm 1.3\text{ mN m}^{-1}$ , which is closed to the previous value. The value of the magnetization  $M(H_{\text{ext}})$  is directly deduced from the magnetization curve of the MF. Taking the latter value of  $\gamma$ , we deduce a capillary length  $l_c=0.12\text{ cm}$ , and the gravitational Bond number  $B_G=0.18$ . The roots of Eq. (14) are reported in Fig. 4 for comparison with the experimental data. Both are qualitatively coherent. We get a good agreement for low values and high values of  $H_{\text{ext}}$ . The discrepancy for the intermediate values should result from the omission of the demagnetizing effect in the magnetic forces.

To take into account this demagnetizing effect, we have to consider an infinite plane with an external field applied perpendicular to the plane. The demagnetizing factor is equal to  $D=1$ . Consequently, the local field is:  $\vec{H}=\vec{H}_{\text{ext}}-D\vec{M}'=\vec{H}_{\text{ext}}-\vec{M}'$ . The magnetization  $\vec{M}'$ , is linked to the local field by the relation  $\vec{M}'=\chi\vec{H}$ , it leads to  $\vec{M}'=(\chi/[1+\chi])\vec{H}_{\text{ext}}$ . A local susceptibility can be determined by the use of the magnetization curve:  $\chi(H_{\text{ext}})=M(H_{\text{ext}})/H_{\text{ext}}$  [47], and subsequently a magnetic Bond number including the demagnetizing effect is

$$B'_M = \frac{\mu_0}{4\pi} \frac{2M'^2 h}{\gamma}$$

We can calculate the contribution of the demagnetizing effects to the theoretical roots. The results are also shown in Fig. 4. The experimental values are between the theoretical predictions  $D=0$  (demagnetizing effects neglected) and  $D=1$  (demagnetizing effects maximized). An exact calculation would have to deal with the nonuniform fringe fields at the edge of a paramagnetic slab.

### B. Growth rates

Now, let us study the growth rate  $\sigma$  of the instability. We measure the length  $\zeta$  of the falling fingers, and divided by  $\zeta_0=\zeta(t=t_0)$ ;  $t_0$  corresponds to the first time where the interface deformation is detectable and is actually given by the resolution of the video recorder. We use a direct measurement of the length instead of a Fourier analysis since it gives results with a huge scattering. Moreover, we have checked that both methods give similar results within the error bars for the wavelength at the onset of the RTI. Plotting this relative depth to which the instability penetrates the lighter fluid as a function of time, we can clearly separate two distinct stages (Fig. 5).

Just after the onset of the instability, when the amplitude of the growth (the length of the spikes) is small compared to the wavelength, we see an exponential growth over time. This occurs for all values of the external applied field. We

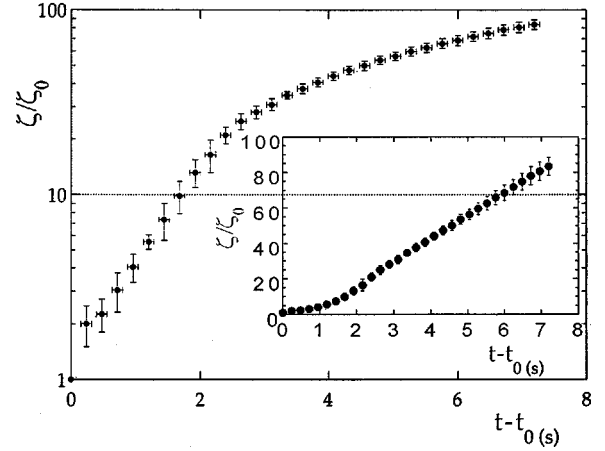


FIG. 5. Growth rates for  $H_{\text{ext}}=23.6\text{ kA/m}$  in the exponential regime and in the linear regime (shown in the inset) as a function of time.

observe an augmentation in the growth rate values as the field increases, as is predicted by the linear analysis given by the formula (12). In this equation, the growth rate is a function of  $H_{\text{ext}'}$  and also a function of  $x_0$ . As we have seen in the previous part,  $x_0$  is an implicit function of  $H_{\text{ext}'}$ , and we cannot find an explicit expression of  $\sigma(H_{\text{ext}})$ . Nevertheless, Eq. (12) can be written

$$\frac{\sigma - \sigma^*}{\bar{\sigma}} = B_M \quad (15)$$

with the growth rate for the mode of wavelength  $\lambda_0=hx_0$  in the absence of magnetic field

$$\sigma^* = \frac{b}{x_0} \left( \frac{B_G}{4\pi^2} - x_0^{-2} \right)$$

and a characteristic inverse of time

$$\bar{\sigma} = \frac{b}{2x_0^3} (a' + \ln x_0).$$

We define  $b=2\pi^3\gamma/3\eta_+h$  and  $a'=1-C_{\text{Euler}}-\ln\pi=-0.72$ , and  $x_0$  is defined previously.

If we insert the theoretical values of the wavelength  $x_0^{\text{th}}$ , in the expressions of  $\sigma^*$  and  $\bar{\sigma}$  we can compare the theoretical linear analysis to the experimental measurements of  $\sigma^{\text{exp}}$ .

These experimental results of the growth rate  $\sigma^{\text{exp}}$  measured near the onset of the instability for different values of the external applied field are shown in Fig. 6, where we plot  $(\sigma^{\text{exp}}-\sigma^*)/\bar{\sigma}$  versus the magnetic Bond number. The theoretical continuous line results from the linear analysis [Eq. (15)] and is the first bisectrix of the Fig. 6. The experimental results are below the theoretical curve, but are included in the error bars. These experimental uncertainties are large due to the difficulty of measuring the amplitude  $\zeta$ .

To reduce the systematic discrepancy between the two curves, we can, as with the wavelength treatment, take into account the demagnetizing field effect. The plot of  $(\sigma^{\text{exp}}-\sigma^*)/\bar{\sigma}$  versus  $B'_M$  is also reported in Fig. 6. In contrast to the previous case, the data are above the first bisectrix. Since

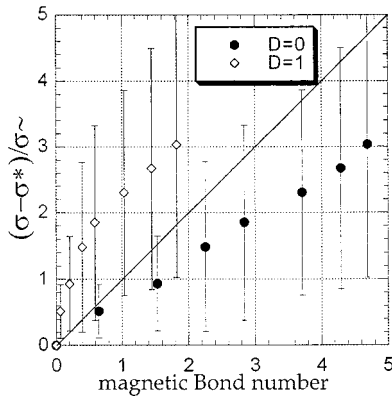


FIG. 6. Magnetic field dependence of the growth rate; black circles represent the experimental data (see text) without demagnetizing effects; white squares maximize the demagnetizing effects in the expression of the magnetic Bond number.

we have crudely included the demagnetizing fields through a demagnetizing factor  $D=1$ , the demagnetizing effects are naturally overestimated, and this explains the intermediate position of the theoretical prediction between the points with  $D=0$  and the ones with  $D=1$ . A fully three-dimensional calculation is needed to properly treat the demagnetization fields at the MF-WS interface.

After the initial exponential growth of the disturbances, we enter a new growth regime shown in the inset of Fig. 5. A linear growth is observed for each value of the applied magnetic field. This behavior is observed for long times, up to the secondary instabilities, where the finger tips split and start to compete with each other. As the magnetic field increases, we observe an increase in the linear coefficient. For example, for  $H_{\text{ext}}=0$ , we get  $\zeta = \zeta_0\{1.9 + 2.0(t-t_0)\}$ , and for  $H_{\text{ext}}=39.3$  kA/m, we get  $\zeta = \zeta_0\{10.8 + 20.1(t-t_0)\}$ . Saturation of the exponential growth is predicted by weakly nonlinear analysis [38]. Crossover from exponential to linear has been found in numerical simulations for nonmagnetic fluids [51].

### C. Far from the threshold

This study emphasized the downward propagating MF fingers, but upward fingers made of WS also exist. As a matter of fact, the heavier liquid, i.e., the MF, falls down due to the buoyancy forces and consequently, the lighter liquid that is the less viscous fluid has to penetrate into the viscous one. A finger of WS grows between each spike of MF. These WS fingers rise like the ST finger propagating in a narrow channel [21]. In fact, both instabilities (RTI and STI) can be described by the same set of equations [38]. The width of the WS fingers is greater than the MF fingers, but a common feature is that the width is a decreasing function of the external magnetic field. Such a symmetry breaking of the interface is related to the viscosity contrast between MF and WS [38].

The tip of the WS fingers splits into two fingers (the so-called “tip-splitting” phenomenon) and the angle between these new fingers is roughly equal to  $90^\circ$ . The evolution of the system exhibits a cascade of tip splitting: each new finger divides itself into two fingers that destabilize themselves while they remain upward. Let us notice that the finger

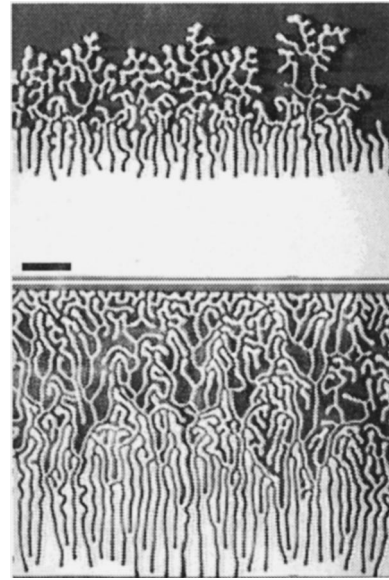


FIG. 7. Pictures of the RTI far from the threshold (see text) and for high value of the applied field:  $H_{\text{ext}}=40$  kA/m. The black bar equals 1 cm.

changes its direction slightly after each tip splitting: it seems to undulate like a narrow finger confined in a channel in the “oscillating-tip” regime [48]. No other secondary instability such as the “side-branching” phenomenon is observed. The tip-splitting cascades acting on a finger give a pattern that looks like a tree as it is illustrated in Fig. 7. This pattern is somewhat similar to the radial viscous fingering obtained with the STI [37] with the difference that the system is anisotropic due to the gravity field.

The MF fingers always remain stable because the viscosity contrast is opposite (a viscous fluid penetrating a less viscous one is stable situation). When the MF fingers are sufficiently far from each other and for high values of the magnetic field, a bending instability occurs [49]. When the distance between the fingers is comparable to the finger width, long range magnetic interactions between fingers are visible: they undulate together for high magnetic field in the same manner than the MF parallel stripes in the bending instability [50]. Finally, the pattern is very non-symmetric [Fig. 7(b)] because of all these features. For high amplitudes of the external field and at long times the top of the cell becomes a labyrinthine and the bottom is rather well organized as the MF smectic [50].

At very long times, the MF accumulates in the bottom of the cell, displacing the WS to the top. The limiting pattern is a conventional MF labyrinth [39] with a reservoir MF at the bottom of the cell (Fig. 8). We investigated whether a hierarchical dynamical behavior [52] emerges because of the treelike structure of highly bifurcated fingers of WS. Retraction of bifurcated fingers cannot occur because their points of bifurcation represent points of force balance and are therefore immobile. To undo a bifurcation requires retraction of at least one of the branches (inset of Fig. 8). However, each branch may itself be bifurcated, further slowing down the pattern evolution. Only at finger tips are forces unbalanced and dynamics unfrozen. Hierarchically constrained dynamics leads to glassy behavior [52]. A Kohlrausch stretched expo-

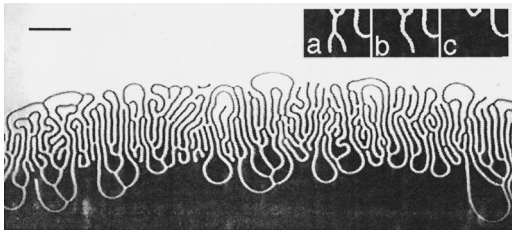


FIG. 8. Final state of the RTI at high fields  $H_{\text{ext}}=40$  kA/m. In the inset, intermediate stage evolution of the RTI (at long time): (a) Arrow points to branched finger about to disappear. (b) 0.5 s later, one branch has retracted. (c) 4 s later, the entire finger disappears. The black bar equals 1 cm.

nential law should govern the evolution in this regime. However, our experiments are consistent with a conventional exponential behavior, at least at short times. In particular, we measured the total interface contour length as a function of time. Over a period of 120 s it fits well to an exponential relaxation with a time constant of 25 s.

## V. CONCLUSION

We perform the Rayleigh-Taylor instability experiment using magnetic fluid. Near the onset of the instability, to describe the pattern, we measure, for different values of the magnetic field, the wavelength and the growth rate of the observed fingers. The magnetic field destabilizes the interface, decreasing the wavelength and increasing the growth rate as it is predicted by the linear analysis of the ferrohydrodynamics equations. We get a good agreement between experiments and theory. At long times, a comparison with numerical simulations for different values of the fields will be of great interest. Other experiments can be performed using a magnetic field applied parallel to the interface in order to stabilize the interface.

## ACKNOWLEDGMENTS

We are greatly indebted to Sophie Neveu for providing us with the magnetic fluid and Patrick Lepert for building the experimental device. We acknowledge useful discussions with Jose Miranda and support by the National Science Foundation Grant No. DMR-9732567.

- 
- [1] Lord Rayleigh, *Scientific Papers II* (Cambridge University Press, Cambridge, England, 1900), p. 200.
- [2] G. I. Taylor, Proc. R. Soc. London, Ser. A **201**, 192 (1950).
- [3] M. Fermigier, L. Limat, J.-E. Weisfreid, P. Boudinet, and C. Quilliet, J. Fluid Mech. **236**, 349 (1992).
- [4] D. H. Sharp, Physica D **12**, 3 (1984).
- [5] L. Smarr, J. R. Wilson, R. T. Barton, and R. L. Bowers, Astrophys. J. **246**, 515 (1981).
- [6] H. J. Kull, Phys. Rep. **206**, 197 (1991).
- [7] S. Chandrasekhar, *Hydrodynamic and Hydromagnetic Stability* (Oxford University Press, Oxford, 1961), Chap. X.
- [8] R. Menikoff, R. C. Mjolsness, D. H. Sharp, C. Zemach, and B. J. Doyle, Phys. Fluids **21**, 1674 (1978).
- [9] M. Mitchner and R. K. M. Landshoff, Phys. Fluids **7**, 862 (1964).
- [10] M. S. Plesset and D.-Y. Hsieh, Phys. Fluids **7**, 1099 (1964).
- [11] R. LeLevier, G. J. Lasher, and F. Bjorklund, Lawrence Livermore Laboratory Report No. UCRL-4459, 1955 (unpublished).
- [12] R. Menikoff, R. C. Mjolsness, D. H. Sharp, and C. Zemach, Phys. Fluids **20**, 2000 (1977).
- [13] K. O. Mikaelian, Phys. Rev. E **47**, 375 (1993).
- [14] A. Elgowainy and N. Ashgriz, Phys. Fluids **9**, 1635 (1997).
- [15] E. Ott, Phys. Rev. Lett. **29**, 1429 (1972).
- [16] L. Baker and J. R. Freeman, Sandia National Laboratories Report No. Sand80-0700, 1980 (unpublished).
- [17] W. P. Crowley, Lawrence Livermore Laboratory Report No. UCRL-72650, 1970 (unpublished).
- [18] P. Petitjeans and P. Kurowski, C. R. Acad. Sci. Paris **325**, 587 (1997).
- [19] J.-R. Authelin, F. Brochard and P.-G. de Gennes, C. R. Acad. Sci. Paris **317**, 1539 (1993).
- [20] J. A. Miranda and M. Widom, Int. J. Mod. Phys. B **12**, 931 (1998).
- [21] P. G. Saffman and Sir G. I. Taylor, Proc. R. Soc. London, Ser. A **245**, 312 (1958).
- [22] S. I. Abarzhi, Phys. Fluids **11**, 940 (1999).
- [23] D. L. Youngs, Physica D **12**, 32 (1984).
- [24] D. L. Youngs, Phys. Fluids A **3**, 1312 (1991).
- [25] K. I. Read, Physica D **12**, 45 (1984).
- [26] M. Ratafia, Phys. Fluids **16**, 1207 (1973).
- [27] P. Gondret and M. Rabaud, Phys. Fluids **9**, 3267 (1997).
- [28] A. Lange, M. Schröter, M. A. Scherer, A. Engel, and I. Rehberg, Eur. Phys. J. B **4**, 475 (1998).
- [29] M. D. Cowley and R. E. Rosensweig, J. Fluid Mech. **30**, 671 (1967).
- [30] A. Cebers and M. M. Maiorov, Magn. Hidrodin. **1**, 127 (1980); **3**, 15 (1980).
- [31] R. E. Rosensweig, M. Zahn, and R. Shumovich, J. Magn. Magn. Mater. **39**, 127 (1983).
- [32] T. Mahr and I. Rehberg, Phys. Rev. Lett. **81**, 89 (1998).
- [33] J. Browaeys, J.-C. Bacri, C. Flament, S. Neveu, and R. Perzynski, Eur. Phys. J. B **9**, 335 (1999).
- [34] J.-C. Bacri, A. Cebers, J.-C. Dabadie, S. Neveu, and R. Perzynski, Europhys. Lett. **27**, 437 (1994).
- [35] J.-C. Bacri, U. d'Ortona, and D. Salin, Phys. Rev. Lett. **67**, 50 (1991).
- [36] M. Zahn and R. E. Rosensweig, IEEE Trans. Magn. **16**, 275 (1980).
- [37] C. Flament, G. Pacitto, J.-C. Bacri, I. Drikis, and A. Cebers, Phys. Fluids **10**, 2464 (1998).
- [38] M. Widom and J. Miranda, J. Stat. Phys. **93**, 411 (1998).
- [39] R. W. Rosensweig, *Ferrohydrodynamics*, (Cambridge University Press, Cambridge, England, 1985).
- [40] D. P. Jackson, R. E. Goldstein, and A. O. Cebers, Phys. Rev. E **50**, 298 (1994).
- [41] A. O. Cebers, Magnetohydrodynamics **16**, 236 (1980).
- [42] *Handbook of Mathematical Functions*, edited by M. Abramowitz and I. A. Stegun (Dover, New York, 1965), p. 375.
- [43] S. Neveu from the Laboratoire des Liquides Ioniques et Interfaces Chargées, located at University Paris 6.

- [44] R. Massart, IEEE Trans. Magn. **17**, 1247 (1981).
- [45] NIH Image by Wayne Rasband, National Institutes of Health available at <http://rsb.info.nih.gov/nih-image/>.
- [46] C. Flament, S. Lacis, J.-C. Bacri, A. Cebers, S. Neveu, and R. Perzynski, Phys. Rev. E **53**, 4801 (1996).
- [47] We use  $\chi(H_{\text{ext}}) = M/H_{\text{ext}}$  instead of  $\chi = M/H$  because it is not possible to measure directly the internal magnetic field.
- [48] Y. Couder, N. Gerard, and M. Rabaud, Phys. Rev. A **34**, 5175 (1986).
- [49] J.-C. Bacri, A. Cebers, C. Flament, S. Lacis, R. Melliti, and R. Perzynski, Prog. Colloid Polym. Sci. **98**, 30 (1995).
- [50] C. Flament, J.-C. Bacri, A. Cebers, F. Elias, and R. Perzynski, Europhys. Lett. **34**, 225 (1996).
- [51] G. Tryggvason and H. Aref, J. Fluid Mech. **154**, 287 (1985).
- [52] R. G. Palmer, D. L. Stein, F. Abrahams, and P. W. Anderson, Phys. Rev. Lett. **53**, 958 (1984).